Troposphere–Planetary Boundary Layer Interactions and the Evolution of Ocean Surface Density: Lessons from Red Sea Corals

GIDON ESHEL, DANIEL P. SCHRAG, AND BRIAN F. FARRELL

Department of Earth and Planetary Sciences, Harvard University, Cambridge, Massachusetts

(Manuscript received 29 August 1997, in final form 23 February 1999)

ABSTRACT

A time series of oxygen isotope ($\delta^{18}O$) measurements of a coral from the northern Red Sea (RS) is presented and used as a direct proxy for water surface density ρ_s. With a relatively constant subsurface density, the generated surface density time series closely tracks water mass formation variability. Two positive and two negative high-amplitude ρ_s anomalies are studied, and associated atmospheric and oceanic data are analyzed to understand large-scale ocean–atmosphere processes. The dominant process is lower-tropospheric subsidence. It dries the boundary layer (BL), increases surface evaporation and ρ_s, and ultimately drives water mass formation. The main cause of the subsidence is a temperature increase along the principal axis of the RS from the eastern Mediterranean to the convergence zone (CZ, 18°–22°N). The increase entails isentropes sloping down to the southeast, crossing pressure surfaces due to their tilt. With nearly adiabatic flow along the principal axis, air parcels move roughly along the sloped isentropes toward ever increasing pressure; that is, they subside. The subsidence supplies the northern RS BL with upstream air from higher altitudes (where humidity is low), thus drying the BL. The resultant high evaporation north of ~25°N (with low evaporation minus precipitation south of ~22°N) depresses sea levels in the northern RS, and thus drives the RS thermohaline circulation and controls water mass formation. Excluded from the presented picture, but probably very important, is mixing with the hot, dry air of the surrounding deserts.

1. Introduction

Gradients of surface density of the ocean (ρ_s) are central to large-scale ocean dynamics, driving thermohaline circulation and controlling water mass formation among other processes. Surface fluxes of heat and moisture determine ρ_s, yet surprisingly little is known about the details and temporal variability of atmosphere–ρ_s coupling. This is primarily due to limited temporal coverage of high-quality ocean–atmosphere observations. (However, the limited information that we do have unambiguously shows that water mass formation rates vary widely in various sites, mostly reflecting ρ_s variability.) One way to alleviate the limited time-coverage problem is to use naturally occurring recorders of sea surface temperature, salinity, or density, validated against instrumental data in some period of overlap, to extend the available records backward in time. The northern Red Sea (RS) is ideally suited for this approach; it is the only place on earth in which deep water forms where corals grow. This permits the application of well-tested geochemical methods to reconstruct past variability of ρ_s and water mass formation. Here we present a coral-derived ρ_s time series for the northern RS, validate its 1974–95 segment against instrumental data, and use both data sources to study coupled configurations in which ρ_s is maximized and deep waters form. The coral-derived ρ_s time series agrees well with instrumental records of surface variables. Fortuitously, two deep hydrographic surveys were conducted before and after the single most extreme coral-derived high-ρ_s anomaly (the winter of 1982/83, during which estimated ρ_s exceeded climatological deep water density). Remarkably, this dataset documents deep water renewal at that time (Woelk and Quadfasel 1996), observationally substantiating our prediction.

We propose a simple theory for regional ocean–atmosphere coupling, whose centerpiece is a subsiding flow from the eastern Mediterranean's middle to low troposphere toward the northern RS boundary layer (BL). This flow supplies the RS BL with dry air, thus causing the unusually high evaporation, and water mass formation. This picture differs markedly from the conventional view of this region's aridity, which emphasizes latitude (i.e., generic, zonally symmetric subtropical subsidence) as the cause for the aridity.

Corresponding author address: Dr. Gidon Eshel, Dept. of Geophysical Sciences, University of Chicago, 5734 S. Ellis Ave., Chicago, IL 60637.
E-mail: geshel@midway-uchicago.edu

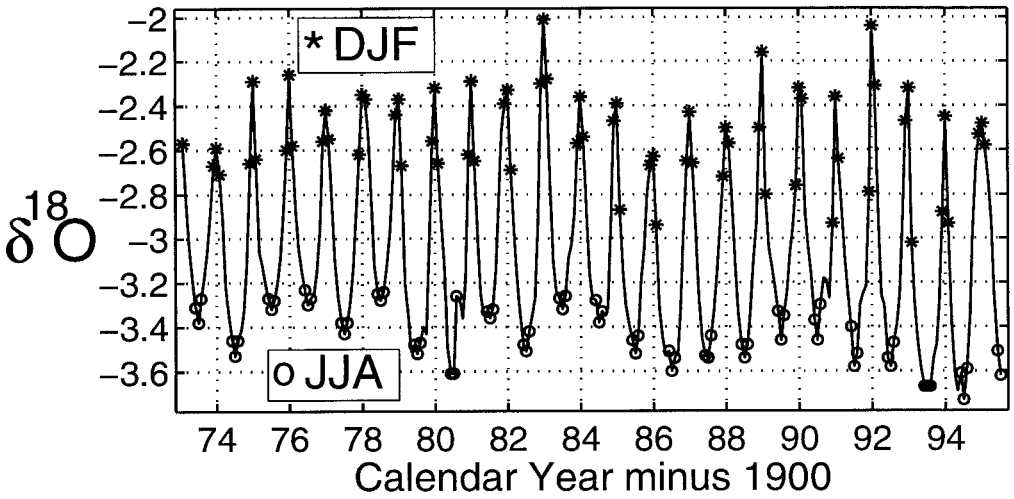

FIG. 1. Oxygen isotopic composition (per mil) of a northern Red Sea (alternate Reef, 27°43′N, 34°07′E, 3-m depth) coral. Asterisks and open circles denote Dec–Feb and Jun–Aug values, respectively. See text for technical details.

The Red Sea: A brief review

Below we summarize some facts about the RS that are relevant to the interpretation of the coral results. For more thorough reviews, see Cember (1988), Eshel (1996), Tragou and Garrett (1997), and Woelk and Quadfasel (1996); for some dynamical ideas about the climatological circulation, see Eshel and Naik (1997) and references therein.

In spite of the low latitude (~26°–27°N), water masses form in the northern RS, primarily due to the basin's geometry and the atmospheric aridity. The atmospheric BL over the Sinai Peninsula and northern RS is intensely dry, but it gradually moistens to the south; until south of ~22°N [the Convergence Zone (CZ)] the BL is already very humid. This humidity pattern is consistent with the climatological atmospheric motions over the RS. While at the CZ air rises from the BL into the free troposphere, over the northern RS and the Sinai Peninsula free tropospheric air subsides into the BL and dries it. The relative humidity patterns give rise to a northward increase of evaporation, up to >2.5 m yr^{-1} at the extreme north of the basin. The cumulative effect of net freshwater loss north of the CZ, compounded with higher evaporation in the north and the northwesterly winds off the Sinai Peninsula, act together to depress the sea level in the northern RS. The resultant northward sea level slope is the primary circulation driver north of the CZ (Cember 1988; Eshel and Naik 1997). For the purpose of the following analysis, the northern RS flow can be idealized as a simple thermohaline overturning cell. At and near the surface, a northward flow loses freshwater and heat (and thus buoyancy) to the atmosphere along its path. At the extreme north during winter, the dense surface water loses additional buoyancy, deep mixing ensues, and the resultant deep pressure gradient drives a return (southward) flow at depth (Cember 1988; Eshel et al. 1994; Woelk and Quadfasel 1996).

While the above climatological picture is suggested by theory and observations (the above references and references therein), the only documentation of time-specific deviations from this mean state is provided by Woelk and Quadfasel (1996) for the winter of 1982/83. No record of formation rates as a function of time exists. Thus a time series of ρ_s (the key dynamical variable for water mass formation) at the RS formation site is essential for a better understanding of temporal variability of formation. Such a time series, derived from coral isotopic composition, is the basis of the current paper.

2. Northern Red Sea data

a. Coral record of seawater density of the northern Red Sea

Previous studies have demonstrated that oxygen isotope records from corals can provide accurate reconstructions of sea surface temperature and salinity (e.g., Cole and Fairbanks 1990; Cole et al. 1993). Several coral genera, particularly *Porites,* construct massive colonies, often 200–400 yr old, which in shallow reef environments may have growth rates on the order of 1 cm yr^{-1}. By sampling at millimeter intervals, a time series may be obtained at approximately monthly resolution.

In order to obtain a time series of ρ_s, we present an oxygen isotope record from a *Porites lutea* coral that we collected from the northern Red Sea (Fig. 1) in the summer of 1996. Cores through several colonies were collected from the Ras Mohammed National Park, at the southern tip of the Sinai Peninsula (27°43′N, 34°07′E). The reefs are directly exposed to the open RS, with abyssal depths reached within 1 km of the sampling sites. This choice provides the best possible

representation of oceanic conditions at a coastal site, with minimal coastal effects.

The δ^{18}O time series (analytical methods are given in appendix A) exhibits large seasonality (1–2 per mil), consistent with the large seasonal cycle of SST. The age model for the coral record is constructed by assigning each δ^{18}O maximum to 15 February, and each minimum to 15 August, roughly consistent with climatological SST extrema. While this assumption may produce slight errors in age assignments, the total error in age is <2 months, too small to present a serious limitation of the presented analyses. The coral isotope record correlates well with nearby ship SST observations, further supporting our assertion that the reef conditions in this location adequately represent the open RS.

A major difficulty with oxygen isotope reconstructions of climate variability has been that the oxygen isotopic composition of the coral skeleton reflects both the temperature and the isotopic composition of ambient seawater. The seawater isotopic composition reflects the net evaporation history of the water, and thus closely covaries with salinity. As water density is our primary interest, this ambiguity is not a problem but rather an advantage because the codependence of δ^{18}O on temperature and salinity allows us to use the δ^{18}O of the coral as a direct measure of seawater density. We convert the δ^{18}O record to a density record using two methods. Although both methods are described in appendix B in detail, a brief summary of each is given here. In the first method, we take advantage of the fact that over the temperature and salinity range in this region, the temperature and salinity dependences of both coral δ^{18}O and water density are very similar, thus supporting a well-defined mapping between δ^{18}O and density. The second method uses the observed correlation between temperature and salinity to reduce the dependence of both density and δ^{18}O to a single variable. The ρ_s time series that are based on these methods (Fig. 2; appendix B) are very similar, with discrepancies well below their expected accuracy. We conclude that Fig. 2 adequately represents northern RS surface density evolution between 1973 and 1995, taking note of both temperature and salinity effects. The density time series shows large interannual variability with pronounced high-density anomalies during 1982/83 and 1991/92 and low anomalies during 1985/86 and 1993/94. Together, these anomalies hold valuable information about the regional ocean–atmosphere system and are thus the focus of the remainder of the paper.

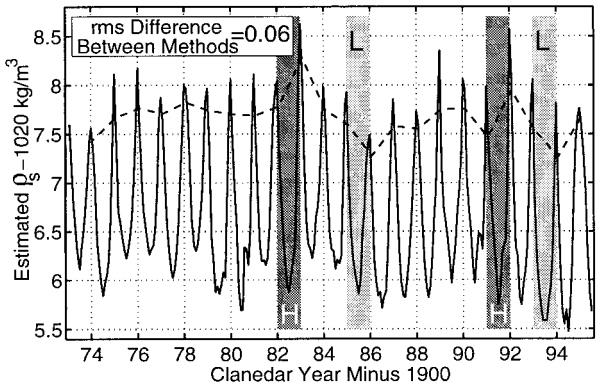

FIG. 2. Conversion of measured $\delta^{18}O_c$ to surface density in the northern RS, as described in appendix B. (The slight disagreement between the two methods is too small to be discernible, with the rms difference given in the upper-left corner). The dashed line show the winter means. The vertical bars show the 1-yr periods that precede the extreme anomalies; the period of RS low-density anomaly is characterized by the mean of the two 1-yr periods (24 months; light shading, L) prior to the 1985/86 and 1993/94 minima, while the period of RS high-density anomaly is characterized by the mean of the 24 months that preceded the 1982/83 and 1991/92 maxima (dark shading, H).

b. Instrumental data

To study the mechanisms of RS ρ_s variability, we supplement the coral information with data from other sources. Most surface information (e.g., SST, sea level air temperature and humidity, and precipitation) is based on the analyzed observations of ships of opportunity (daSilva et al. 1994). Tropospheric variables (above the BL; winds, humidity, temperature) are taken from the National Centers for Environmental Prediction–National Center for Atmospheric Research (NCEP–NCAR) 40-Year Reanalysis Project (Kalnay et al. 1996). The reanalysis data are not ideally suited for our purpose, as they are not purely observed, but rather represent assimilation of observations into a state-of-the-art atmospheric GCM. While a blend of observed and modeled data is inferior to high-quality, high-(spatial and temporal) resolution observations, such a dataset does not currently exist; there is not enough station data to calculate dynamical fields (such as divergence) accurately. On the other hand, the model's thermodynamics are strongly constrained by data in the RS region [e.g., a 34-yr record of spatial (over the northern RS) and seasonal (December–March) mean 1000-mb air temperature from the reanalysis data correlates >0.9 with its daSilva counterpart]. Hence, the dynamically consistent assimilated fields, while clearly imperfect, are the best currently available approximation to the true fields. Errors related to transient features are averaged out in the monthly mean data we use and are further reduced by the 24-month averaging period that we employ (see below). Similarly, the characteristic space scales for the anomalies analyzed here are fairly large [typically $O(10 \times 10$ grid points)] and are thus relatively immune to small-scale noise in the assimilation model. Given the above, our results, and the data-driven theory we present below, should be considered tentative, awaiting perfection of the observational network.

We average anomalies from these data over the two 1-yr periods (24 months combined) preceding the two high-ρ_s anomalies, and construct a canonical configuration that describes the state of the RS during high-ρ_s

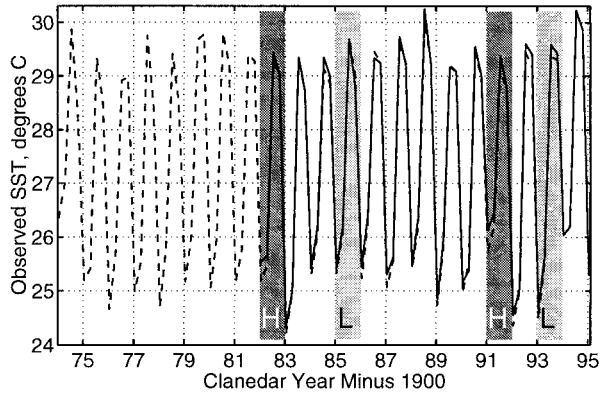

FIG. 3. Observed SST averaged over the northern RS (20°–29°N, 33°–42°E). From 1974 until mid-1993 (dashed line) the data are from daSilva et al. (1994); from 1982 until 1995 (solid line) the data are from the IGOSS analysis (Reynolds and Smith 1994). The shaded areas show the 1-yr periods preceding the calculated ρ_s anomalies.

anomaly (hereafter ρ_s^{HIGH}). Similarly, we average anomalies in the two 1-yr periods that preceded the two low-ρ_s anomalies to construct a low-ρ_s counterpart, ρ_s^{LOW}. The 1-yr time integral is taken to represent the timescale over which the upper ocean adjusts to anomalous atmospheric forcing (sections 1a and 3). The time integration is also applied to enhance the robustness of the results by making them less sensitive to precise age determination and transient model noise.

3. Analysis of extreme density anomalies

While the time resolution of Fig. 2 is too coarse to resolve individual short-lived high-density (and thus water mass formation) events, the figure still contains some valuable information about water mass formation. First, the climatological annual-mean lower-thermocline (250 m) density of $\sigma_\theta \simeq 28.2$ kg m^{-3} [based on temperature and salinity of 21.9°C and 40.15 practical salinity units (psu), respectively (Cember 1988; Eshel et al. 1994)] is exceeded in the winters of 1982/83, 1988/89, and 1991/92. Based on static stability considerations, renewal of the lower thermocline (and possibly deeper depths) occurred during those periods. While we do not have information about the latter periods, the prediction regarding 1982/83 is confirmed by Woelk and Quadfasel's (1996) demonstration of deep water renewal in the northern Red Sea between October 1982 and May 1983.

Another useful preliminary check of Fig. 2 is a comparison with observed spatial-mean SST variability, shown in Fig. 3. Clearly the ρ_s calculations are in good agreement with observed SST; the two high-ρ_s cases are also the two coldest winters in the record, and 1993/94 is the warmest one. While 1985/86 is also a warm winter, it is not as extreme. Similarly, the 1990/91 warm winter is not registered by the coral as an anomalously low-ρ_s season. These slight discrepancies between the SST and ρ_s records highlight the subtle yet important role of salinity in determining ρ_s; since salinity information does not exist, we cannot investigate this further.

Ship observations from the periods preceding the extreme anomalies (Fig. 4; daSilva et al. 1994) further support Fig. 3. The maps of Fig. 4e–h show anomalously low (high) air and sea surface temperatures throughout the region prior to ρ_s^{HIGH} (ρ_s^{LOW}). This is consistent with the ρ_s anomalies and suggests that the anomalies are partly thermal. With assumed salinity of 40 psu and SST of 25°C, cooling of 1°C (characteristic of maximum cooling during ρ_s^{HIGH} winters) corresponds to a $\delta\rho_s \approx 0.31$ kg m^{-3}. The anomalous seasonal surface latent heat loss (daSilva et al. 1994) during the 1982/83 and 1991/92 winters was 22 and 26 W m^{-2} above the mean (the two highest anomalies), consistent with the above SST anomalies. (But the ρ_s^{LOW} winters were near normal.) The enhanced evaporation that gave rise to the unusually high latent heat fluxes during ρ_s^{HIGH}, $O(0.2$ m yr$^{-1})$, increases ρ_s not only by cooling the upper ocean, but also by making it saltier. To quantify the latter effect, consider a 50-m-thick upper layer with initial uniform salinity of 40 psu. Upon losing 0.2 m to evaporation, the layer's salinity increases to 40.2 psu. With a temperature of 25°C, this salinity increase corresponds to $\delta\rho_s \approx 0.15$ kg m^{-3}, approximately half the thermal effect. Together, the thermal and haline effects add to a total $\delta\rho_s$ of nearly 0.5 kg m^{-3}, similar to the calculated values (Fig. 2).

Relative humidity anomalies (Figs. 4a,b) are negative (positive) prior to ρ_s^{HIGH} (ρ_s^{LOW}) throughout the RS, consistent with BL drying triggering the enhanced evaporation during ρ_s^{HIGH}. To estimate the effect of the relative humidity change, let evaporation E (in m s^{-1}) be $\rho_a\rho_w^{-1}C_E\|\mathbf{u}\|(q_s - q)$ (Gill 1982), where the symbols represent, respectively, air and water density ($\rho_a\rho_w^{-1} \approx 1.2 \times 10^{-3}$), a dimensionless transfer coefficient ($\sim 1.5 \times 10^{-3}$, Gill 1982), wind speed (~ 10 m s^{-1}), and the difference between the saturation and actual specific humidities. Also (with a trivial error), let the relative humidity r be $100q/q_s$, and assume nearly constant temperature (and thus q_s), such that $E \approx \rho_a\rho_w^{-1}C_E\|\mathbf{u}\|q_s(1 - 0.01r)$. Then $\delta E = -0.01\rho_a\rho_w^{-1}C_E\|\mathbf{u}\|q_s\delta r$ is the finite evaporation change in response to a finite relative humidity change δr. Taking $q_s \sim 0.025$, $\delta r \sim 1\%$ and the above numerical values, yields $\delta E \simeq 0.14$ m yr^{-1}, close to the observed ~ 0.2 m yr^{-1}. The difference is attributable to small changes in q_s, wind speed, temperature, etc. The large fraction of the observed evaporation change that is due to relative humidity variability emphasizes the importance of this variability in yielding the observed oceanic surface density anomalies.

Precipitation anomalies prior to ρ_s^{HIGH} (Fig. 4d) are negative throughout the RS, consistent with the ρ_s anomaly, and with suppression of moist ascent. While precipitation anomalies prior to ρ_s^{LOW} (Fig. 4c) are positive in the southern RS, as expected from the ρ_s anomaly, they are strongly negative in the north, near the retrieval site. Also, the negative precipitation anomaly prior to

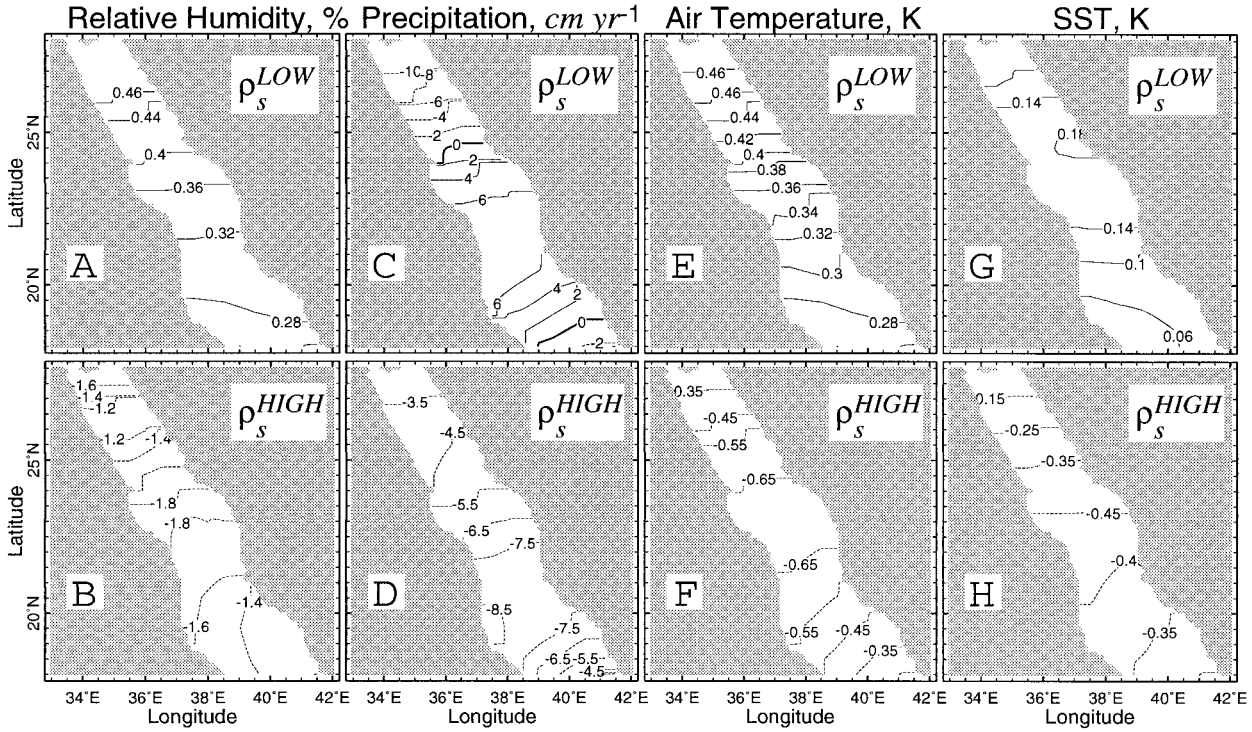

FIG. 4. Time-mean anomalies of observed oceanic and boundary layer properties in the northern Red Sea prior to coral-derived Red Sea low (upper) and high (lower) surface density anomalies. Negative contours are dashed. From daSilva et al. (1994) data.

ρ_s^{HIGH} peaks near the CZ, and not near the retrieval site. This is consistent with the RS general circulation outlined in the review. Northern RS surface water is renewed from the south on an $O(1\ \mathrm{yr})$ timescale by northward surface flows. These flows integrate RS-wide anomalous forcing and transmit the resultant ρ_s perturbations up the channel to the northern RS, where they are recorded by the corals. The effect of the observed $\sim$0.03 m season^{-1} precipitation anomalies is rather small; for the same 50-m thick mixed they correspond to $\delta S \approx 0.02$ psu, or (for a temperature of 25°C), to $\delta\rho_s \approx 0.02$ kg m^{-3}, $\sim$10% of the evaporation effect.

Thus, ship observations support the existence of ρ_s anomalies at the times suggested by Fig. 2 and show that both thermal and haline effects on ρ_s are important; cold, dry conditions yield ρ_s^{HIGH}, and warm, humid spells produce ρ_s^{LOW}. To explain the anomalies, a proposed mechanism should simultaneously account for cooling and drying (or warming and moistening).

Because reduced relative humidity occurs in colder conditions, the reduction must be due to decreased specific humidity q, by either (horizontal or vertical) advection, or surface fluxes. As discussed above, estimated anomalous evaporation prior to ρ_s^{HIGH} (when q was anomalously low) was about twice as high as prior to ρ_s^{LOW}. Since from the elevated surface evaporation we would have expected unusually moist conditions during ρ_s^{HIGH}—opposite to the observed—we must conclude that anomalous evaporation is not the cause of the humidity change, but rather a response to it. Clearly q must be modulated by advection, and the advecting winds must be related to observed three-dimensional gradients of q and θ (the air potential temperature) so as to cool while drying.

We show below that the northern RS is strongly cooled, but weakly moistened or dried, by horizontal advection (the climatological northern RS annual and spatial mean horizontal moisture transport is very nearly zero). Consequently, while horizontal advection variability is a prime candidate for explaining the thermal part of the ρ_s anomalies, it cannot explain the drying; we must look for moisture sinks elsewhere. One possibility is the surrounding dry deserts, but the mixing scale is too fine to be resolved by our data. Since $\partial_p q \gg \|\nabla q\|$, a potentially important q sink is subsidence of dry air from aloft into the BL. Anomalies of BL wind divergence, a better-observed subsidence surrogate (Fig. 5), are therefore particularly illuminating in the analysis of RS ρ_s anomalies.

Perturbations of BL wind divergence prior to RS ρ_s anomalies are strong and are almost mirror images of each other. This supports the idea that subsidence modulations force ρ_s anomalies. Both extremes peak near the CZ (19°–22°N) and maintain coherence throughout the northern RS. The dry and cold conditions of ρ_s^{HIGH} accompany anomalously strong subsidence; whereas the moist, warm BL during ρ_s^{LOW} occurs while subsidence is weakened. This is further substantiated by Fig. 6,

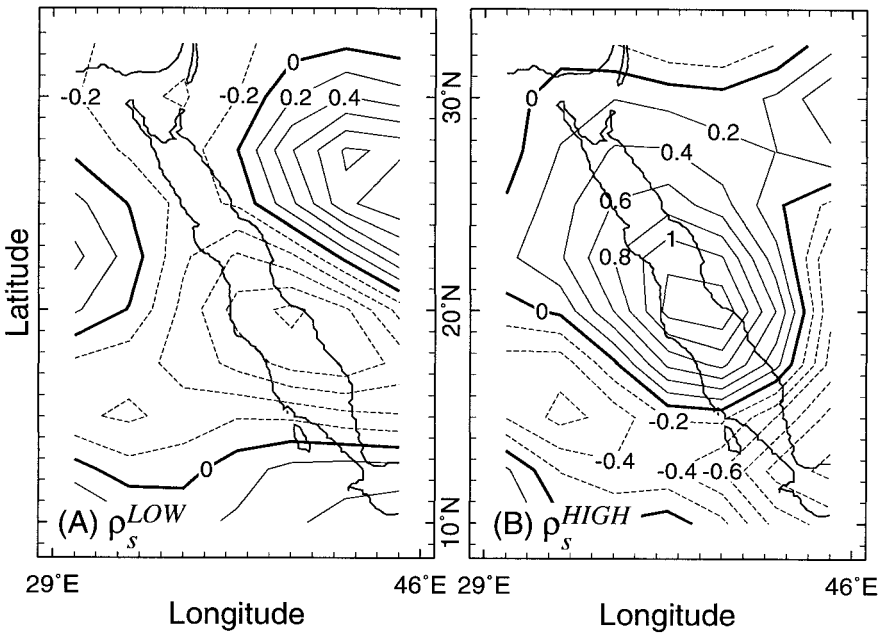

FIG. 5. Anomalies of 925-mb wind divergence from the NCEP–NCAR reanalysis data (Kalnay et al. 1996) in 10^{-6} s^{-1}. The average conditions prior to the RS (a) low-density and (b) high density anomalies. See text for time-averaging details.

which shows that both high-ρ_s years correspond to seasonal- and annual-mean subsidence maxima (or ascent minima). The situation during low-ρ_s events, when the anomalies are smaller, is more ambiguous. The events do not coincide with subsidence minima, but 1993/94 is the global minimum of annual-mean subsidence. Also, while 1985/86 is low, it is not a clear minimum. Clearly, subsidence is not the sole determinant of ρ_s, but it controls the high-ρ_s events, during which water masses are most likely to form in the extreme northern RS.

To fit all observations into a coherent, self-consistent framework, we need to understand the dynamics of RS subsidence and their interactions with horizontal advection.

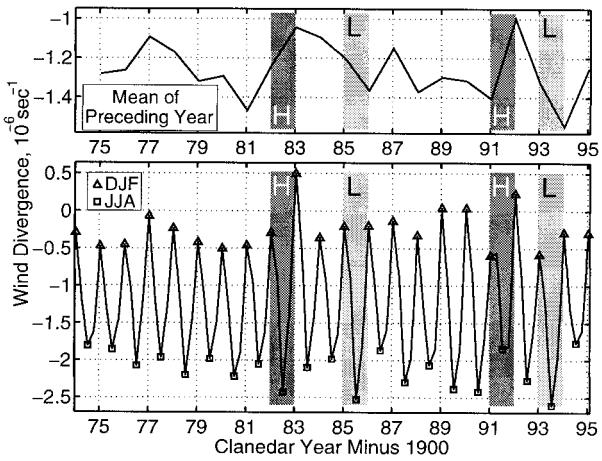

FIG. 6. Time series of spatial-mean (over 15°–30°N, 33°–44°E) 925-mb horizontal wind divergence: (lower) Seasonal means, with winter and summer values indicated by the symbols; (upper) the mean divergence during the 12 months preceding each winter. (For example, the February 1990 data point represents the Mar 1989–Feb 1990 mean.) Higher positive divergence values correspond to intensified subsidence. From the reanalysis data (Kalnay et al. 1996).

4. A simple theory for Red Sea subsidence

To analyze the subsidence and its variability, we focus on the relatively homogeneous lowest 150 mb (~1.5 km), and employ a control surface at 850 mb, which any motion between the BL and the troposphere must cross. Since we consider vertical motions and buoyancy, we replace θ with the virtual potential temperature of the air, θ_v, which accounts for the effect of water vapor on air density.

a. Climatology

Figure 7 shows the lower-troposphere annual-mean climatological flow, q and θ_v. Northwesterlies from the eastern Mediterranean (EMD) nearly parallel the temperature gradient over the northern RS, and thus transport heat extremely efficiently. Anomalies about these means are sufficiently small, such that upon decomposition to (overbarred) means and (primed) fluctuations, $\|\overline{\mathbf{V}} \cdot \nabla\overline{\theta}\| \gg (\|\mathbf{V}' \cdot \nabla\overline{\theta}\|$ and $\|\overline{\mathbf{V}} \cdot \nabla\theta'\|)$ always. Thus the right-hand panel of Fig. 7 shows that horizontal winds always cool (to a variable degree) the northern

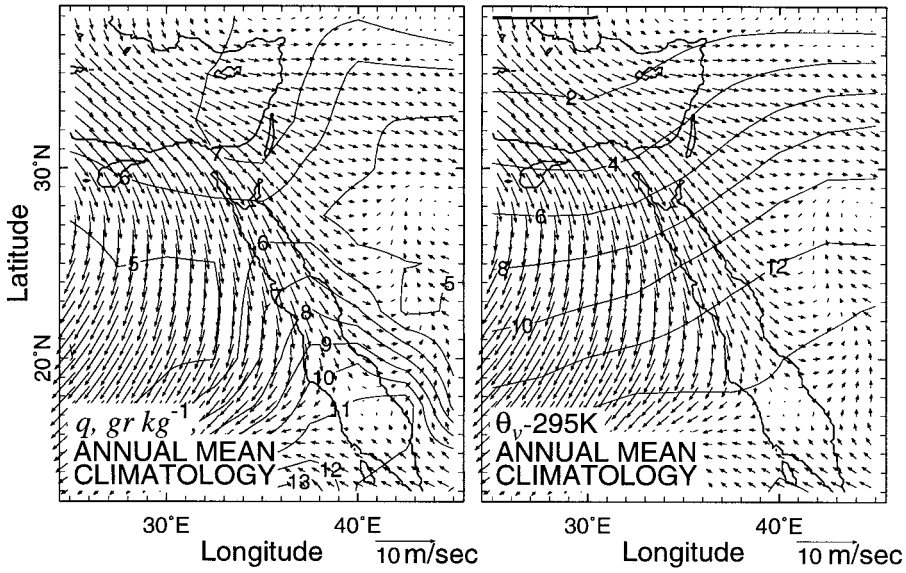

FIG. 7. Annual-mean lower-troposphere ($p > 850$ mb) climatological flow, q and $\theta_v - 295$ K from the NCEP–NCAR reanalysis data (Kalnay et al. 1996). The wind field is repeated in both panels.

RS. The magnitude of the cooling can be estimated as $c_p h \rho_a \mathbf{V} \cdot \nabla\theta$, where c_p and ρ_a are the heat capacity and density of the air, respectively; h is the flow thickness; and $\mathbf{V}$ is the wind. With $h \simeq 4.3$ km (the relevant properties do not change markedly from the configurations shown in Fig. 7 until that height), $\langle \mathbf{V} \rangle \simeq 5$ m s^{-1} (where the angled brackets denote time and 3D space averaging), $\langle \rho_a \rangle \simeq 0.87$ kg m^{-3}, and $\nabla\theta \simeq 11$ K (1800 km)$^{-1}$; the horizontal heat advection is $\sim$115 W m^{-2}, as large as other leading terms in the sea surface thermodynamic balance such as radiative or latent heat fluxes. Thus horizontal advection is well worth studying in detail in an effort to explain the ρ_s anomalies.

To this end, let the space coordinates $\tilde{x}$ and $\tilde{y}$ align with the RS axis and across it (positive to the northwest and northeast, respectively). The balances over the northern RS are then

$$\frac{\partial}{\partial t}\left(\frac{\overline{\theta_v}}{\overline{q}}\right) \simeq -\overline{\tilde{u}}\frac{\partial}{\partial \tilde{x}}\left(\frac{\overline{\theta_v}}{\overline{q}}\right) - \overline{\omega}\frac{\partial}{\partial p}\left(\frac{\overline{\theta_v}}{\overline{q}}\right) - \frac{\partial}{\partial \tilde{y}}\left(\frac{\overline{\tilde{v}'\theta_v'}}{\overline{\tilde{v}'q'}}\right) + \frac{1}{\rho_a h}\left[\frac{\overline{\dot{Q}}c_p^{-1}}{(\overline{E - P})\rho_w}\right]. \quad (1)$$

In Eq. (1) we assume dry processes, that the coordinate-rotation makes horizontal advection unidirectional, $\tilde{u}$ and $\tilde{v}$ are the flows along $\tilde{x}$ and $\tilde{y}$, ω is the vertical velocity with respect to pressure p, $\dot{Q}$ is heating in Watts per meter squared, $E - P$ is the net surface evaporation rate in meters per second, and $\rho_w = 1000$ kg m^{-3} is water density. Overbarred quantities are slowly evolving, while the third rhs term represents mixing by mean correlations between high-frequency fluctuations. This term accounts primarily for mixing of hot and dry desert air into the RS atmosphere by ageostrophic land/sea breezes, which develop in response to large diurnal temperature gradients across the RS shores. Consequently, we retain the term in the $\tilde{y}$ direction only. Unfortunately, the limited space scales that our dataset resolves do not permit us to say anything about the magnitude or variability of this term; its absence inevitably renders any of the following budgets incomplete. Focusing on the heat budget and permitting only down-channel advection for the moment, with (from Fig. 7) characteristic $\tilde{u} \simeq -5$ m s^{-1}, $\delta\theta_v \simeq -11$ K and $\delta\tilde{x} \simeq 1800$ km, $\partial_t\theta \simeq -2.6$ K day^{-1}. Obviously such a tendency cannot be maintained and must be balanced by the neglected terms. The diabatic term comprises radiative and surface heat fluxes, both small compared to the advective heating. Further, these terms only worsen matters by some additional cooling, indicating that $\dot{Q}$ is unlikely to balance the heat budget. Aside from unresolved boundary mixing, the heat budget is roughly closed by subsidence:

$$-\overline{\tilde{u}}\frac{\partial\overline{\theta_v}}{\partial\tilde{x}} \simeq \overline{\omega}\frac{\partial\overline{\theta_v}}{\partial p} \quad (2)$$

or $\overline{\omega} \simeq -\overline{\tilde{u}}\,\partial_{\tilde{x}}\overline{\theta}_v(\partial_p\overline{\theta}_v)^{-1}$. With the above numerical values, and lower troposphere $\partial_p\overline{\theta}_v \simeq -3.6$ K (100 mb)$^{-1}$ over the northern RS, this formula yields $\overline{\omega} \simeq 70$ mb day^{-1}, while the observed annual mean climatological subsidence is 40–60 mb day^{-1}. This discrepancy is expected given the high level of idealization of Eq. (2). It consists of eddy-correlation heating, which limits subsidence; surface cooling, which enhances subsidence; and the small resulting upward moisture transport, which suppresses subsidence. Note that the above adiabatic analysis is by necessity incomplete and merely illustrative, as diabatic and synoptic processes can play

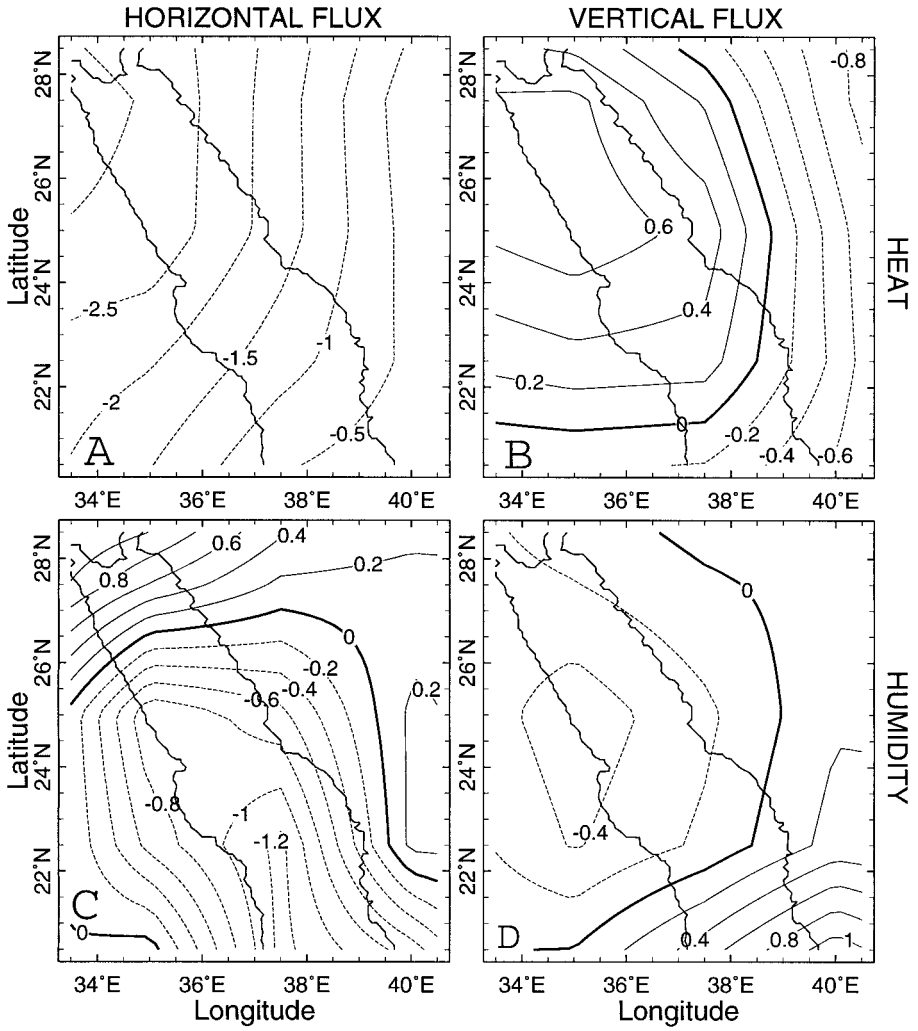

FIG. 8. Leading terms in the annual mean climatological lower troposphere ($p \geq 850$ mb) [(a) and (b)] heat, and [(c) and (d)] humidity budgets. (a) and (c) show the horizontal component, $-(\overline{u}\partial_x + \overline{v}\partial_y)$; (b) and (d) show the vertical component, $-\overline{\omega}\partial_p$.

important roles in the full climatological dynamics as well but are neglected here.

To corroborate the above analysis, Figs. 8a and 8b show the observed mean advective heat flux divergences in the lowest ~1.5 km. Cooling by horizontal advection (Fig. 8a) peaks (<-3 K day^{-1}) at the extreme north and decreases in magnitude downstream. Consistent with Eq. (2), subsidence heating (Fig. 8b) follows the same general pattern but is smaller. The imbalance between horizontal and vertical advective heating is most likely closed primarily by mixing with the surrounding hot deserts. Unfortunately, as discussed above, this mixing is too finescaled to be resolved by our data, and we cannot address it quantitatively.

Figure 9 extends vertically the information of Fig. 7. The θ_v surfaces sequentially intersect the 850-mb surface, which they are higher than to the north and lower than to the south. Taken together, Figs. 7 and 9 illustrate the subsidence mechanism, which is similar to the mechanism that Rodwell and Hoskins (1996) advance to explain upper-tropospheric subsidence due to stationary waves. To the extent that the flow is near-adiabatic ($Q \simeq 0$), isentropes are materially impenetrable; air parcels on a given isentrope over the EMD will remain on this isentrope as the parcels are advected down the RS. Due to the downstream temperature increase, a small yet nonzero angle exists between θ and p surfaces (between the solid curves and the horizontal dotted and dashed lines of Fig. 9). As a result, θ-conserving motions (which follow the solid curves of Fig. 9 from upper-left to lower-right) cross constant-p surfaces (such as the 850-mb dashed line) toward higher pressure; that is, they subside. Thus, northern RS subsidence arises when near-adiabatic flows from the EMD down the RS encounter baroclinic lower troposphere.

Humidity is secondary in the theory of climatological

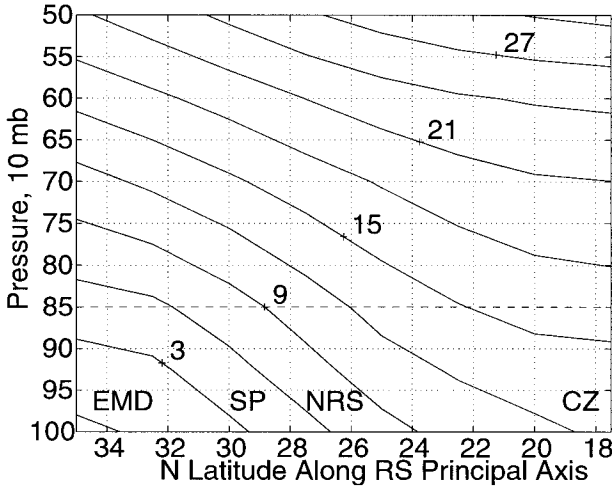

FIG. 9. Annual-mean lower-tropospheric $\theta_v - 295$ K climatology along the principal axis of the RS. The horizontal dashed line shows the 850-mb surface, CZ is the climatological convergence zone, NRS the northern RS, SP the Sinai Peninsula, and EMD the eastern Mediterranean. From the reanalysis data (Kalnay et al. 1996).

subsidence, as it is mostly passively advected by the flow, rather than actively modifying it like the temperature field. However, humidity is central to the anomalies that drive ρ_s variability (section 3). Figure 7 shows that climatologically, horizontal winds are not nearly as potent in advecting moisture as they are in advecting heat; ∇q is small and has a saddle point over the northern RS, such that only south of ~25°N the down-channel winds encounter q larger than EMD values. In sharp contrast to the clear control that horizontal advection exerts over the temperature tendency, the magnitudes of horizontal and vertical moisture advection are similar. Furthermore, north of ~25°N, horizontal advection actually moistens, adding to moistening by surface evaporation.

Thus in the northern RS climatology, evaporation is unusually high due to drying by both subsidence and mixing with nearby deserts. Consequently, subsidence is associated with both BL cooling (by horizontal advection, which drives the subsidence in the first place, and also by enhanced evaporation) and drying (by downward advection of dry air). As discussed in section 3, the coolness–dryness association is the fundamental requirement for explaining the ρ_s anomalies, and the subsidence mechanism meets this criterion simply and naturally.

b. Extreme anomalies

Our interest in the anomalies about the presented climatology is twofold. First, we seek further evidence for subsidence control of RS ρ_s. Second, for completeness, we need to describe the mechanisms through which subsidence anomalies interact with the underlying ocean to yield the ρ_s anomalies. Figures 10 and 11 show the relevant anomalies, in analogy to Figs. 7 and 8, and further corroborate the idea that ρ_s^{LOW} and ρ_s^{HIGH} represent two opposite extremes in which, in addition to the upper ocean, both the RS BL and the regional lower troposphere undergo rearrangement.

Prior to ρ_s^{HIGH}, $\partial_{\tilde{x}}\theta_v$ is more negative than normal between the EMD and the CZ, while the down-channel winds are anomalously strong ($\tilde{u}$ anomalously negative; Fig. 10d). Conversely, prior to ρ_s^{LOW}, $\partial_{\tilde{x}}\theta_v$ is less negative than normal, and the down-channel winds are weakened (Fig. 10b). In both ρ_s^{LOW} and ρ_s^{HIGH} the $\tilde{u}$ and $\partial_{\tilde{x}}\theta_v$ anomalies affect advective cooling and subsidence intensity in the same direction [$\overline{\tilde{u}}\,\partial_{\tilde{x}}\theta_v'$ and $\tilde{u}'\,\partial_{\tilde{x}}\overline{\theta}$ are of the same sign, while $\tilde{u}'\partial_{\tilde{x}}\theta'$ is always negligible; see Eq. (2)]. From Figs. 10b and 10d we expect anomalously strong (weak) cooling by horizontal advection prior to ρ_s^{HIGH} (ρ_s^{LOW}); this is indeed shown by Figs. 11a and 11c (with anomalies roughly an order of magnitude smaller than the climatological values). Based on the discussion in section 4a, these anomalies should be accompanied by intensified (weakened) subsidence prior to ρ_s^{HIGH} (ρ_s^{LOW}). Again, this is exactly what Fig. 5 shows. Figures 11e and 11g show the resultant anomalous vertical advective heating, which opposes the horizontal one in both ρ_s^{LOW} and ρ_s^{HIGH}. The partial cancellation of lateral and vertical advective fluxes in both the anomalous and climatological states further emphasizes the $\overline{\omega} \simeq -\overline{\tilde{u}}\,\partial_{\tilde{x}}\overline{\theta}_v(\partial_p\overline{\theta}_v)^{-1}$ interconnection. In both ρ_s^{LOW} and ρ_s^{HIGH} (as well as in the climatology), cooling by horizontal advection drives RS lower-troposphere subsidence, which in turn shapes BL humidity, surface evaporation, ρ_s, and ultimately the thermohaline circulation of the RS.

As discussed in section 3 and shown in Fig. 10c, the low relative humidity prior to ρ_s^{HIGH} (Fig. 4b) is due to anomalously low q. Figures 11d and 11h show that this dryness is mostly the result of the intensified subsidence, especially at ~24°–27°N. As shown in section 3, the low humidity, and by implication the enhanced subsidence, affect ρ_s both by enhancing evaporation and by suppressing moist ascent (thus limiting precipitation; note the spatial correspondence of the extrema in Figs. 4d and 11h).

During ρ_s^{LOW} the picture is generally reversed. The anomalously high relative humidity (Fig. 4a) is due to elevated q (Fig. 10a) in response to weakened down-channel winds (Fig. 10a) and subsidence (Fig. 5a). The weakened down-channel winds permit dilution of northern RS ambient dry air with moist CZ air, while the reduced subsidence yields below-normal drying. Thus in the anomalies, as in the climatology, the heat field is the primary force behind the subsidence, while the ensuing humidity redistribution is the primary forcing agent of the ocean. Together, they yield the ρ_s variability (Fig. 2).

5. Conclusions and summary

This paper argues for a direct control of Red Sea surface density by large-scale lower-tropospheric mo-

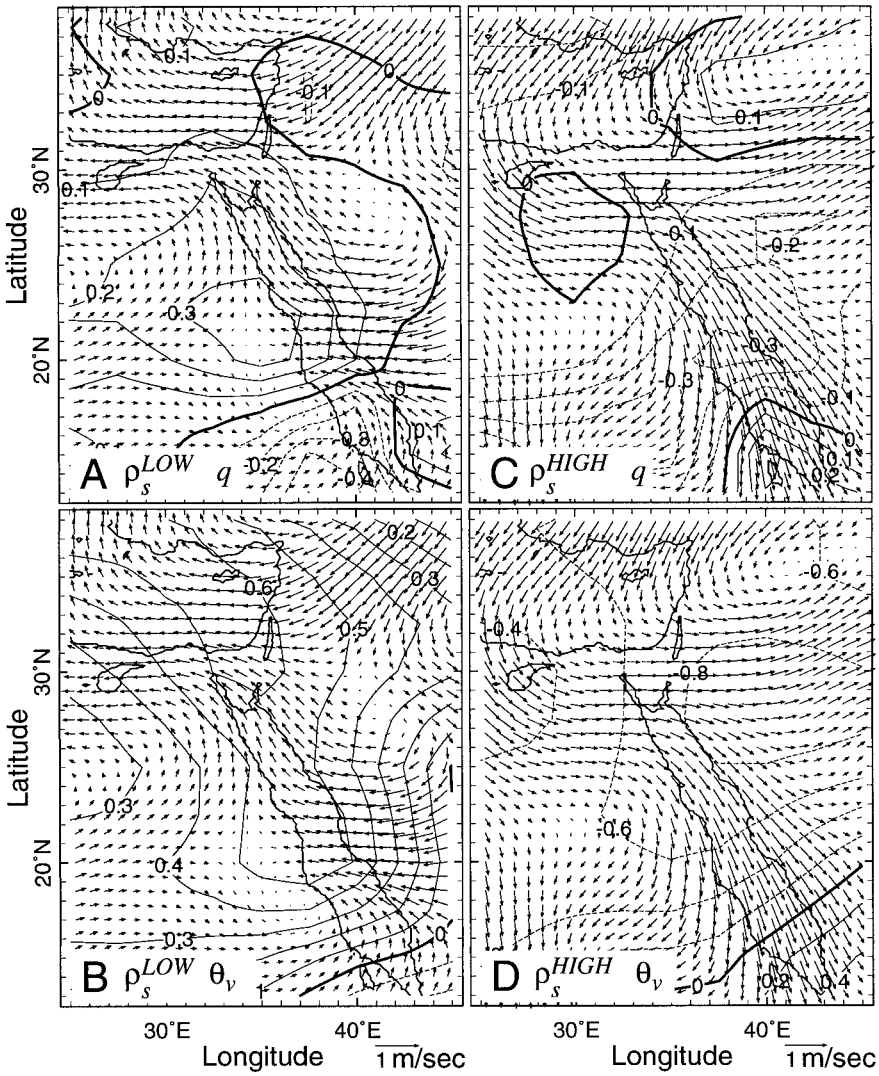

FIG. 10. Lower-troposphere ($p \geq 850$ mb) wind (m s^{-1}; scale vectors below lower panels), θ_v (K; lower) and q (g kg^{-1}; upper) anomalies prior to ρ_s^{LOW} (left) and ρ_s^{HIGH} (right). Negative contours are dashed. From the reanalysis data (Kalnay et al. 1996).

tions. Based on both data and theory, we suggest that lower-tropospheric subsidence and the associated flux of dry free troposphere air into the boundary layer are the key processes. By drying the lowermost atmosphere of the northern Red Sea, subsidence increases surface evaporation and ocean density, thus controlling water mass formation. While subsidence is extremely powerful in modifying the humidity field, its main cause is a temperature increase along the principal axis of the northern Red Sea. The increase causes isentropes to slope down to the southeast and sequentially intersect pressure surfaces. To the extent that the flow along the principal axis is nearly adiabatic, it roughly follows the sloped isentropes. This means that as air flows southward down the channel, it flows toward ever increasing pressure, that is, it subsides. [Subsidence can also be viewed as providing the heating (by adiabatic compression) that is necessary to oppose cooling by downchannel horizontal winds along the temperature gradient toward higher temperatures.] The descending flow puts boundary layer air at any given point along the northern Red Sea downstream of air from aloft, which is considerably drier. This advective drying is what makes subsidence so powerful in controlling surface density. The sharp contrast between the high-evaporation environment at 23°–28°N, and surface moisture convergence, low surface evaporation, and lower-tropospheric moist ascent (i.e., precipitation) south of ~22°N sets up a climatological sea surface slope to the north. This slope, with extreme northern RS sea levels up to 50 cm below that at 20°N, is the principal driver of RS thermohaline circulation and water mass formation.

Ocean–atmosphere anomalies are consistent with the above climatological picture; anomalously strong sub-

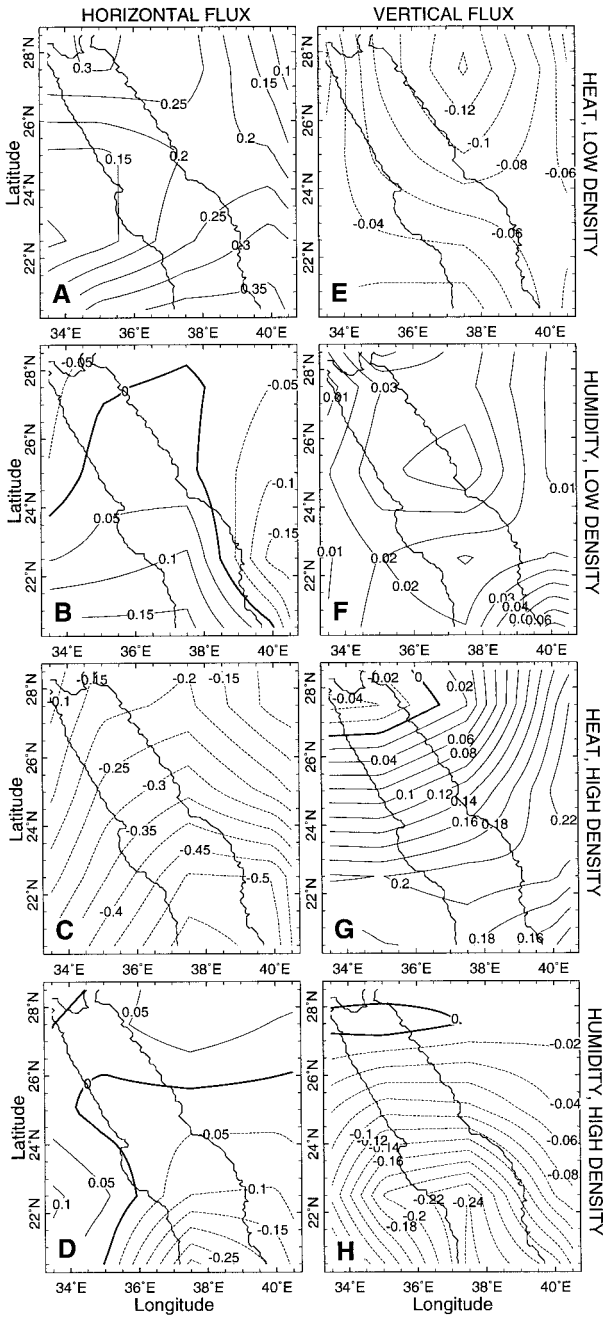

FIG. 11. Leading terms in the anomalous lower-troposphere ($p \geq$ 850 mb) heat (rows 1, 3) and water vapor (rows 2, 4) budgets prior to ρ_s^{LOW} (rows 1, 2) and ρ_s^{HIGH} (rows 3, 4). The left and right columns are $-(\overline{u}\partial_x + \overline{v}\partial_y)$ and $-\overline{\omega}\partial_p$ of $\overline{\theta}_v$ (in K day^{-1}; rows 1, 3) and $\overline{q}$ (in g kg^{-1} day^{-1}; rows 2, 4), respectively. From Kalnay et al. (1996). See Fig. 8 for more details.

sidence is followed by unusually high surface density, and (to a lesser extent) below-normal surface density follows weakened subsidence. Because of large-scale processes that are beyond the scope of this paper, downchannel winds vary temporally. As they intensify, for example, so does subsidence (because of the need to balance enhanced horizontal advective cooling). The increased advection of low-humidity air from the lower free troposphere further dries the boundary layer. The reduced relative humidity, along with the intensified winds, drives up surface evaporative cooling and lower SSTs. In all steady states (and the analyzed anomalous states are persistent enough to be considered steady) subsidence drying always opposes moistening of the boundary layer by evaporation, and subsidence heating opposes cooling by horizontal winds. The coincidence in 1982/83 of strong cooling by horizontal winds, intensified subsidence, dryer than usual boundary layer, and finally water mass formation in the northern Red Sea (Woelk and Quadfasel 1996) powerfully demonstrates the above ties.

Thus the proposed mechanism combines and reconciles observed oceanic, boundary layer, and atmospheric anomalies into a unified, internally consistent dynamical picture that explains the temporal variability of coral-derived surface density.

Acknowledgments. We thank Michael Moore for supervising the field expedition, Jean Lynch-Steiglitz for sharing the idea behind the $\delta^{18}O_c \rightarrow \rho_s$ conversion, and three anonymous reviewers, whose comments strengthened the paper considerably. This work was supported by NSF (OCE-94-16712 and OCE-94-16895). Eshel was supported by a UCAR/NOAA Climate and Global Change fellowship, and by the Woods Hole Oceanographic Institution.

APPENDIX A

Analytical Methods

The cores were split, and a 1-cm-thick slab was taken from the center. Samples were taken at 1-mm increments using a low-speed drill. Approximately 1 mg of each sample was loaded into a stainless steel capsule, placed in an automated carbonate preparatory system, and then reacted in orthophosphoric acid at 90°C. The CO_2 was analyzed on a gas-source mass spectrometer. Precision based on measurements of standard calcite spaced throughout each run averages 0.04 ppm for $\delta^{18}O$.

APPENDIX B

Conversion Methods for $\delta^{18}O_c \rightarrow \rho_s$

This section describes the two methods we use to convert the oxygen isotope record to seawater density. The first method exploits the fact that there exist empirical analytic expressions for the T and S dependence of both density and equilibrium $\delta^{18}O_c$. The former is simply the equation of state of seawater, but the latter is less straightforward. Andrie and Merlivat (1989) used seven surface RS samples and concluded that $\delta^{18}O_w^{\text{SMOW}} = 0.291S - 9.787$ (where the superscript SMOW identifies the reference, standard mean ocean

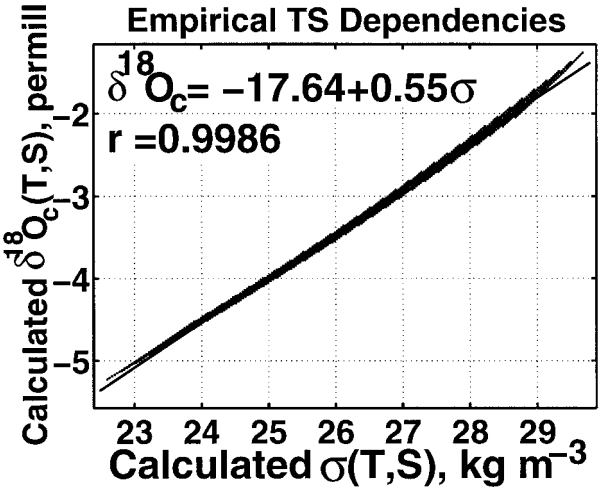

FIG. B1. The relationship between $\delta^{18}O_c$ and σ ($\sigma \equiv \rho - 1000$) as a function of temperature (T) and salinity (S). Each dot represents a given choice of a T–S combination, mapped to σ (using the equation of state for seawater) and to $\delta^{18}O_c$ (using an analytic expression that combines thermodynamic and empirical considerations, as described in the text). As the correlation coefficient r shows, the two signals are practically redundant in the RS-relevant T–S range (which spans the figure), such that the regression expression can be used to calculate σ from $\delta^{18}O_c$.

water, about which the $\delta^{18}O$ values are calculated). Craig (1966) used surface, intermediate, and deep RS waters, and suggested $\delta^{18}O_w^{SMOW} = 0.29S - 9.85$. We take intermediate values, $\delta^{18}O_w^{SMOW} = 0.29S - 9.81$, or, upon conversion to the PDB standard that we use hereafter, $\delta^{18}O_w = 0.281S - 39.452$. This, along with the temperature dependence of $\delta^{18}O_c$ (O'Neil et al. 1969), yields

$$\delta^{18}O_c = 0.281S - 42.342 + 2.78 \times 10^6\, T_K^{-2} - D, \quad \text{(B1)}$$

where T_K is the temperature in Kelvins and D accounts for isotopic disequilibrium that the coral maintains with the ambient water, which will be quantified below. Using the equation of state and Eq. (B1) we can compute both density and $\delta^{18}O_c$ for any arbitrary T–S combination. With T and S values that span the entire observed ranges, we can estimate the expected $\sigma(T, S)$–$\delta^{18}O_c(T, S)$ relationship ($\sigma \equiv \rho - 1000$), as quantified by the regression expression of Fig. B1.

The correlation between $\sigma(T, S)^{calc}$ and $\delta^{18}O_c(T, S)^{calc}$ [where the superscript ''calc'' refers to values that were calculated using the equation of state and Eq. (B1)] is >0.99. That is, completely fortuitously, in the T–S ranges that are relevant to the RS, the empirical dependencies of both ρ and $\delta^{18}O_c$ on T and S yield essentially interchangeable signals; knowing ρ closely determines $\delta^{18}O_c$, and vice versa. This is by no means the general case, and will fail in other T–S regimes. The high correlation should therefore not be overinterpreted, as it depends strongly on the T–S ranges over which the correlation is being calculated. It is visually clear from Fig. B1 that the correspondence is only local (in T–S space), and as the T–S ranges expand, the correlation deteriorates rapidly. [The deterioration occurs because within the hydrographic range of the Red Sea (20°–30°C, 37–41 psu),

$$\frac{\partial\sigma}{\partial S}\left(\frac{\partial\sigma}{\partial T}\right)^{-1} \simeq \frac{\partial\delta^{18}O_c}{\partial S}\left(\frac{\partial\delta^{18}O_c}{\partial T}\right)^{-1} \sim O(1),$$

while, to use a rather extreme example, for $T = -1$°C and $S = 25$ psu

$$\frac{\partial\sigma}{\partial S}\left(\frac{\partial\sigma}{\partial T}\right)^{-1} \simeq 122 \times \frac{\partial\delta^{18}O_c}{\partial S}\left(\frac{\partial\delta^{18}O_c}{\partial T}\right)^{-1},$$

demonstrating the strictly local nature of the density–$\delta^{18}O_c$ correlation.]

From the fit of $\delta^{18}O_c$ to σ in the Red Sea T–S ranges shown in Fig. B1, we obtain

$$\delta^{18}O_c = -17.642 + 0.546\sigma, \quad \sigma \equiv \rho - 1000, \quad \text{(B2)}$$

which can be used to invert measured $\delta^{18}O_c$ values for density, namely,

$$\sigma = 0.546^{-1}(17.642 + \delta^{18}O_c^{measured}). \quad \text{(B3)}$$

Equation (B3) is the first method by which we convert measured $\delta^{18}O_c$ to density.

The second conversion method exploits the observed T–S relationship. It is a common observation throughout most of the ocean that some T–S combinations are more likely than others. That is, a given T value suggests a corresponding S value, and vice versa, such that the dimensionality of the equation of state is reduced to 1. The degree to which this relationship holds varies, but it is the the rationale behind the very fundamental concept of ''water masses.'' North of 26°N, there exist 28 surface winter observations of both T and S. The casts are distributed throughout the winter months without a preferred clustering and are located mostly along the shipping routes from the central axis of the RS to the Gulfs of Eilat and Suez. The T–S correlation in these casts is -0.83. While not perfect, this correlation indicates that in the northern RS, temperature and salinity are indeed related to some degree, as expected, such that their empirical relationship

$$T = 177.77 - 3.83S \quad \text{(B4)}$$

is expected to be somewhat useful. Even though the rms error about this fit is quite large, 0.455°C, it corresponds (with $S = 40$ psu and $T_0 = 23$°C) to density variability of only $\sim$0.1 kg m^{-3}. Since this is $\sim$5% of the observed density range, we proceed with the analysis and later examine its validity and usefulness a posteriori.

With $T = T(S)$, Eq. (B1) becomes

$$\delta^{18}O_c = 0.281S - 42.342 + 2.78 \times 10^6(K_0 + 177.774 - 3.834S)^{-2} - D, \quad \text{(B5)}$$

where $K_0 = 273.15$ K, the origin of the Celsius scale,

and, as before, D accounts for isotopic disequilibrium. Since Eq. (B5) is nonlinear in S, it cannot be explicitly solved for S by analogy to Eq. (B3), but it can be readily solved iteratively. The second method by which we convert measured $\delta^{18}O_c$ to density is thus to iteratively solve Eq. (B5) for S, then solve Eq. (B4) for T, and finally use the equation of state to convert the calculated T and S to density.

To close both methods we must quantify D of Eqs. (B1) and (B5). We do not have any time information about the amplitude of the isotopic disequilibrium, so we take it to be stationary and equal to the deviation of the mean observed $\delta^{18}O_c$ from the calculated equilibrium one using the observed mean T and S, $\overline{T}$ and $\overline{S}$,

$$D = 0.281\overline{S} - 42.342 + 2.78 \times 10^6(K_0 + \overline{T})^{-2} - \overline{\delta^{18}O_c^{\text{measured}}} = 3.05 \text{ per mil.} \quad \text{(B6)}$$

REFERENCES

Andrié, C., and L. Merlivat, 1989: Contribution des données isotopiques de deutérium oxygène-18 hélium-3 et tritium, à l'étude de la circulation de la Mer Rouge. *Oceanol. Acta,* **12,** 165–174.

Cember, R. P., 1988: On the sources, formation, and circulation of Red Sea deep water. *J. Geophys. Res.,* **93** (C7), 8175–8191.

Cole, J. E., and R. G. Fairbanks, 1990: The Southern Oscillation recorded in the $\delta^{18}O$ of corals from Tarawa atoll. *Paleoceanography,* **5** (5), 669–683.

——, ——, and G. T. Shen, 1993: Recent variability in the Southern Oscillation: Isotopic results from a Tarawa atoll coral. *Science,* **260,** 1790–1793.

Craig, H., 1966: Isotopic composition and origin of the Red Sea and Salton Sea geothermal brines. *Science,* **154,** 1544–1548.

daSilva, A., A. C. Young, and S. Levitus, 1994: *Algorithms and Procedures.* Vol. 1, *Atlas of Surface Marine Data 1994,* NOAA Atlas NESDIS 6, U.S. Department of Commerce.

Eshel, G., 1996: Coupling of deep water formation and the general circulation: A case study of the Red Sea. Ph.D. thesis, Columbia University, 127 pp.

——, and N. Naik, 1997: Climatological coastal jet collision, intermediate water formation, and the general circulation of the Red Sea. *J. Phys. Oceanogr.,* **27,** 1233–1257.

——, M. A. Cane, and M. B. Blumenthal, 1994: Modes of subsurface, intermediate, and deep water renewal in the Red Sea. *J. Geophys. Res.,* **99** (C8), 15 941–15 952.

Gill, A. E., 1982: *Atmosphere–Ocean Dynamics.* International Geophysical Series, Vol. 30, Academic Press, 662 pp.

Kalnay, E., and Coauthors, 1996: The NCEP/NCAR Reanalysis Project. *Bull. Amer. Meteor. Soc.,* **77,** 437–471.

O'Neil, J. R., R. N. Clayton, and T. K. Mayeda, 1969: Oxygen isotope fractionation in divalent metal carbonates. *J. Chem. Phys.,* **51,** 5547–5558.

Reynolds, R. W., and T. M. Smith, 1994: Improved global sea surface temperature analyses. *J. Climate,* **7,** 929–948.

Rodwell, M. J., and B. J. Hoskins, 1996: Monsoons and the dynamics of deserts. *Quart. J. Roy. Meteor. Soc.,* **122,** 1385–1404.

Tragou, E., and C. J. R. Garrett, 1997: The shallow thermohaline circulation of the Red Sea. *Deep-Sea Res.,* **44,** 1355–1376.

Woelk, S., and D. Quadfasel, 1996: Renewal of deep water in the Red Sea during 1982–1987. *J. Geophys. Res.,* **101** (C8), 18 155–18 165.